An advanced numerical model of friction stir welding of DH36 steel

AL-MOUSSAWI, M., SMITH, Alan <http://orcid.org/0000-0001-7868-8501>, YOUNG, Andrew E, FARAJI, M. and CATER, S.

An Advanced Numerical Model of Friction Stir Welding of DH36 Steel

***[1] Al-moussawi M., * Smith A., *Young A., **Faraji M., ***Cater S.**
***Sheffield Hallam University/UK, **University of Derby, ***(TWI)**
***[1]b1045691@my.shu.ac.uk**

A numerical model of Friction Stir Welding (FSW) of DH36 steel plate (6mm thickness) has been developed using a CFD technique. Two welding speed conditions were used, a low welding speed of 200 RPM - 100mm/min, and a high welding speed of 550RPM- 400 mm/min. The heat generation, material flow and strain rate were calculated based on plastic deformation and frictional contact between the tool and workpiece. A CFD-based model has been produced to represent the asymmetry in temperature distribution between the advancing and retreating side, the material flow and the strain rate. The geometry of the model includes the tool plunged into the plate. The cooling system was also included in the simulation by calculating the heat flux lost for each part of the tool. The heat generated by viscous dissipation away from the tool was also taken into account. The total heat generated was divided into the individual tool parts (shoulder, probe side and probe end) and was found to be in good agreement with the experimental results for the areas affected by these parts. The maximum temperature obtained for the slow welding speed was 1012^{o}C and for the high welding speed was 1250^{o}C. Experimental metallographic examination has also been carried out on DH36 FSW steel plates to validate the CFD model. SEM analysis showed the formation of a fine microstructure of bainite, acicular ferrite and ferrite/cementite aggregate in the welded zone as compared to the ferrite/pearlite morphology in the base metal. It is found from the CFD and experimental results that the high speed welding conditions can produce defects such as wormholes and cracks in the welds associated with the probe side and probe end due to the lack of material flow especially on the advancing side. Tensile and fatigue testing were carried out for both slow and high welding speed samples, which broke outside the welded region in the tensile test, however, slow welding speed samples show more resistance to fatigue test and survived 644128 cycles, the high speed welding samples failed after 111,736 cycles under the same load.
Keywords: FSW, DH36 steel, CFD.

Introduction

Friction stir welding (FSW) is a joining technique which was invented at the DEFINE TWI (TWI) in 1991 and used to join two pieces of metal by mechanical means without fusion or filler materials [Zhang and Zhang 2009]. The technique includes plunging a specially designed rotating tool with a shoulder and terminating in a threaded pin (probe) into the adjoining edges of the work- pieces with a suitable tilt angle, and then traversing linearly along the joint [Barnes et. al. 2012]. The method has been used widely to join many difficult-to-weld alloys such as aluminium-alloys and magnesium, copper and dissimilar alloys. The advantages of FSW include the availability to weld thicknesses ranging from a fraction of millimetre to a third of a meter [Cui et. al. 2007] and to do so in a single pass. The process introduces very little distortion, eliminates porosity and segregation in the weld zone and generally produces a refined, wrought microstructure in the weld zone. However, the method is limited to welding low melting temperature alloys such as aluminium because of the tool requirements and the associated cost. Great interest has been shown in recent years in FSW of a special type of steel grade used for ship building, namely DH36 grade. The commercial use of FSW for DH36 steel grade is still limited because of the high tool cost. There have been many efforts to make FSW process feasible for welding this grade of steel by investigating the beneficial effects of FSW on microstructure and mechanical properties after welding. Toumpis et. al. 2014 (a) performed a technical and economic investigation of the FSW for DH36 steel. They found a profound improvement in both mechanical and microstructure properties when welding by FSW process was compared with Submerged Arc Welding (SAW). However, the tool life has remained an obstacle for the commercial use as the tool represents 99% of the machine's direct cost. Thomas et. al. 1999 have studied the feasibility of FSW for two types of steel (12% chromium alloy and low carbon steel) by investigating the microstructure and mechanical properties. They found mechanical properties and

microstructures of the joints for both steel grades compared well with the parent material. McPherson et. al. 2013 made a comparison between single and double sided FSW of DH36 steel plate by evaluating microstructure and mechanical properties such as hardness, tensile strength, toughness of the joints. They found double-sided FSW joints presented superior properties compared with the single sided joints. They also compared the FSW process with the SAW of the same grade of steel. They reported that both single- and double-sided FSW angular and longitudinal distortion is lower than those in SAW. Toumpis et. al. 2014 (b) investigated the microstructure and mechanical properties of FSW DH36 steel at a wide range of rotational and traverse tool speeds. Their study aimed to find the suitable welding speeds to optimise the properties of the welded joint. They found that slow travelling speed (100-200 mm/min) produced a refined ferrite-rich microstructure; while intermediate traverse speed (250-400 mm/min) produced a pre-dominantly acicular bainitic ferrite, the high travelling speed (500mm/min) produced a heterogeneous microstructure. Their study did not investigate the defects which may form when traverse speed increases. Lienert et. al. 2003, studied the feasibility of FSW of DH36 steel by investigating mechanical properties and microstructure phase changes after the welding. They found a significant improvement in yield strength and hardness of FS welded samples compared with the parent material. The microstructure of the stirred zone was converted to acicular ferrite compared with ferritic and pearlitic bands in the parent metal. Small defects were found in the Stir Zone (SZ) which was attributed to the lack of bonding. Reynold et. al. 2003, discussed the relationship between FSW parameters and properties of 6.4 mm DH36 steel by applying different travelling speeds (204 mm/min, 306 mm/min, 456 mm/min) with constant weld pitch (1.72 rev/mm). They found that microstructure and mechanical properties were improved in the SZ compared to the parent material; however, a defect (wormhole) at the advanced side was formed. From the phase transformation of DH36 they suggested that the temperature of FSW process always exceed the A_3 line on the Fe-C equilibrium phase diagram. There are some efforts on modelling of FSW of DH36 steel grade to be able to estimate the best welding parameters that can improve the microstructure and mechanical properties of the joints and in turn can prolong the tool's life. Despite the fact that FSW involves complex parameters such as tool rotational/traverse speeds, plunge depth, tool tilt, clamping/backing accessories and forces applied which can be an obstacle to controlling the process; however, modelling using CFD can effectively capture these difficulties. A review of numerical modelling of FSW can be found in Xiaocang et. al. 2014, which mostly include modelling of aluminium, with limited focus on steel. Toumpis et. al. 2014 (c), carried out hot compression testing on DH36 samples in the temperature range of 700-1100°C and strain rate of 0.001-100 s^{-1} in order to calculate the equivalent stress equation parameters. Then they applied these data in 3D thermo-mechanical CFD modelling based on an Eulerian framework. The heat generated was mainly from plastic deformation and frictional heating. The peak temperature at low welding speed (200RPM, 100 mm/min) was 1050°C while for high welding speed (500RPM ,400 mm/min) was 1250°C. The strain and strain rate was also calculated. Although the peak temperatures between numerical modelling and experimental results were in agreement, the model did not investigate the occurrence of defects associated with traverse speed and also the asymmetry between advancing and retreating side was not clear. Nandan et. al. 2007, applied the CFD technique to simulate the FSW of mild steel. They used flow stress and viscosity equations from previous work on steel extrusion. The sticking/sliding parameter based on tool radius was used to represent the spatial distribution of heat flux as a result of plastic and friction heating. From numerical analysis they estimated a range of viscosity from 10^{-5} to 9.9×10^{6} Pa.s in which the material adjacent to the tool can flow. Micallef et. al. 2015 used a CFD model to predict the influence of tool speeds on the shape of SZ and the heat power of FSW DH36. The results of temperature from numerical analysis were in good agreement with thermocouples data. They found that a non-linear variation connects the total heat generation with tool radial and angular positions. Their model did not discuss formation of defects and also did not show a significant asymmetry between advancing and retreating sides especially for high welding traverse speed. In this paper a CFD technique has been used to simulate the FSW of DH36 with two welding conditions, slow and high rotational and traverse speeds, (200RPM, 100 mm/min and 550RPM, 400mm/min, respectively). The heat generated has been represented by plastic/frictional action of the tool on the workpiece at the contact region. The viscosity was taken from a previous work carried out on extrusion of mild steel [Nandan et. al. 2007]. The microstructure was also investigated to study the

effects of changing of the welding parameters. Axial tensile and fatigue tests were also applied on the welded samples according to the British standard.

Materials and numerical method

Two friction stir welded plates of DH36 steel 500 x 400 x 6 mm and 1000 x 800 x 8 mm were provided by TWI which were welded by a hybrid PCBN-WRe tool with the following welding conditions: 550 RPM and 400 mm/min (high speed welding process) and 200RPM, 100 mm/min (low welding speed).

The chemical composition of DH36 from the manufacturer is shown in Table 1. Thermal properties for the workpiece (DH36 steel), shown using the following equations, are presented as function of temperature which are taken from a previous work carried out on low carbon manganese steel [Samuels 1999]:

$$k = 23.16 + 51.96.e^{-2.03T/1000}$$

$$Cp = 689.2 + 46.2.e^{3.78T/1000} \quad for\ T < 700°C$$

$$Cp = 207.9 + 294.4.e^{1.41T/1000} \quad for\ T > 700°C$$

$$\rho = \frac{7850}{[1+0.004\left(\frac{T}{1000}\right)^2]^3}$$

where k, C_P and ρ are thermal conductivity, the specific heat capacity and density, respectively.

Table 1: The chemical composition of DH36 steel grade provided by Masteel UK Ltd..

DH36 Chemical Composition (The Element Max. wt.%)												
C	Si	Mn	P	S	Al	Nb	V	Ti	Cu	Cr	Ni	Mo
0.16	0.15	1.2	0.01	0.005	0.043	0.02	0.002	0.001	0.029	0.015	0.014	0.002

FSW tool of PCBN-WRe with a shoulder radius of 12.5mm and a pin base radius of 5mm and 6mm length was used in the process. The PCBN tool, as shown in Fig. 1, is hybrid and includes a shank made of Tungsten Carbide (WC) and both PCBN (Poly Crystalline Boron Nitride) and shank were surrounded by a collar made of Ni-Cr alloy. The thermal properties for the PCBN hybrid tool are shown in table 2 [Endo et. al. 2010] [MegaStir 2013]:

Table 2: Material properties of the hybrid PCBN parts.

Tool part	thermal conductivity k $W.m^{-1}.K^{-1}$	Specific heat Cp $J.Kg^{-1}.K^{-1}$	Density ρ $Kg.m^{-3}$	Ref.
Shoulder PCBN-WRe	120	750	3480	MegaStir 2013
Shank (WC)	92	500	14900	MegaStir 2013
Collar	11	440	8900	Endo et. al. 2010

The geometry and CFD model assumptions

To make the analysis robust and avoid threads problem in modelling [Ulysse et. al. 2002], smooth tool parts surfaces were designed in Pro-Engineer software and then converted to ANSYS-Fluent. The

designed area for the tool without threads represented the actual area with threads; the Infinite Focus Microscope (IFM) was used to calculate the actual surface area of the threaded tool.

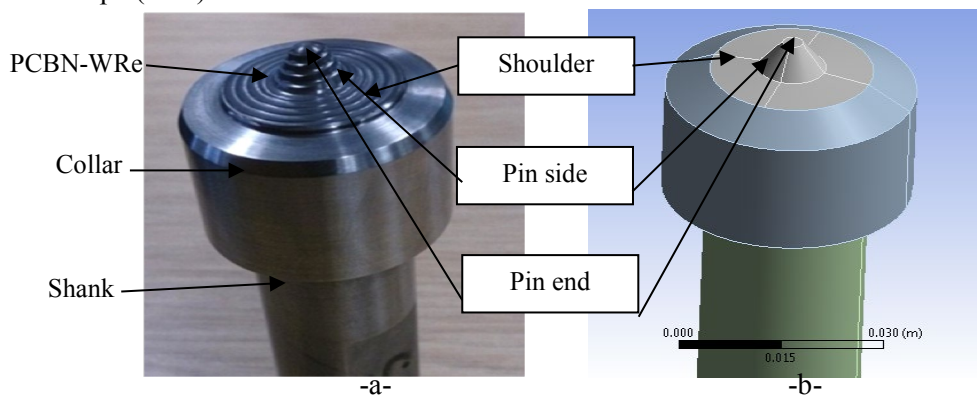

Figure 1: The PCBN Tool .a-Real Image. b- FEM model.

Because of the low thermal conductivity and the small Heat Affected Zone (HAZ) in steel, the plate was designed as a disc with 100mm radius centred on the tool rotational axis as shown in Figure 2 –a [Atharifar et. al. 2009, Toumpis et. al. 2014 (c), Jacquin et. al. 2011 and Grujicic et. al. 2010]. The tool and plate were in a direct contact condition. The backing plate was not represented but a thermal convection with a high value (2000 $W/m^2.K$) was applied on the bottom surface of the plate [Micallef et. al. 2015], this is to increase computation efficiency.

Model assumption:

Non-Newtonian viscosity and laminar flow were assumed and the values of viscosity were taken from a range between a minimum and maximum experimental values of viscosity produced in a study on the extrusion of steel [Nandan et. al. 2007].

-Eulerian framework has been used and the tool is located within the plate (in the welding position). The connection between the tool and the plate was achieved by treating the domain geometry as a single part (Figure 2a). The other side of the plate was assigned with constant pressure and extended far downstream of the tool to ensure there would be no reverse flow at this boundary [Hasan et. al. 2015]. All plate walls were assumed to move with the same speed of the interior (no slip conditions) with zero shear stress at the walls.

-Heat was generated mainly from plastic deformation and friction. This has been achieved by applying the plastic/frictional heat flux as a user defined function UDF in the contact region [Idagawa et. al. 2014].

-Meshing quality as shown in Figure 2b was very high (skewness < 0.3 , aspect ratio < 5 and orthogonality > 0.7), and a very fine tetrahedral mesh was used in the tool/plate contact surface in order to be able to capture the high change in velocity, temperature, strain rate and all the of the physical properties of the steel.

-The tooling of FSW was water-cooled, and in modelling the cooling system was included and represented as a negative heat flux. The loss of heat from the workpiece was represented through application of heat transfer coefficient on the top and bottom walls of the workpiece.

-The tool rotational speed (RPM) was effectively applied in the contact region between the tool and the workpiece. This gave the material in the contact region asymmetry from the retreating to the advancing side as the material flow.

The viscous forces affecting the material were very high, so the gravitational forces were neglected [Atharifar et. al. 2009].

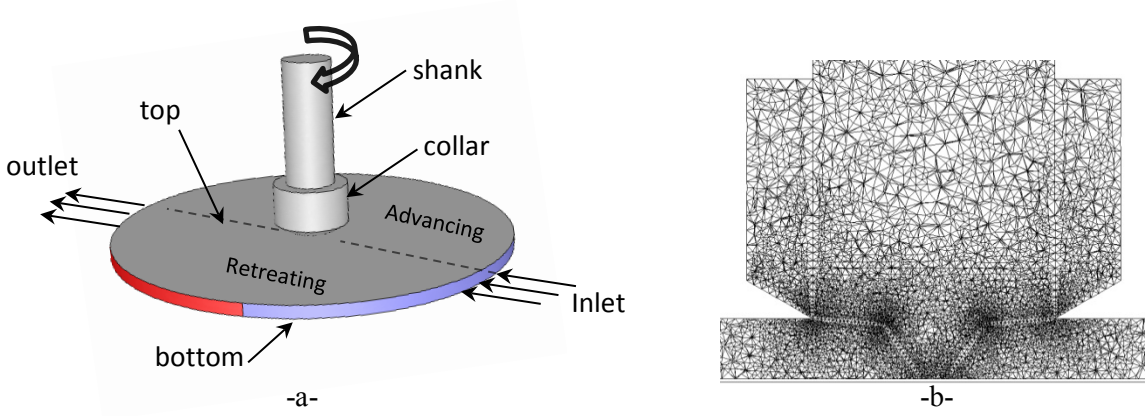

Figure 2 : a- Geometry and boundary conditions . b- Traverse section showing the mesh.

The governing equations:

As the material under study was incompressible, there was no change expected in material properties due to pressure and so the change was considered only as a function of temperature. The continuity equation can be represented as [Nandan et. al. 2007]:

$$\frac{\partial u_i}{\partial x_i} = 0 \qquad (1)$$

u_i is the velocity of plastic flow in index notation for i=1,2 and 3 which representing the Cartesian coordinate of x,y and z respectively.

The temperature and velocity field were solved assuming steady state behaviour. The plastic flow in a three dimensional Cartesian coordinates system can be represented by the momentum conservation equation in index notation with i and j=1,2 and 3, representing x,y and z respectively [Nandan et. al. 2007]

$$\rho \frac{\partial u_i u_j}{\partial x_i} = -\frac{\partial p}{\partial x_j} + \frac{\partial}{\partial x_i}\left(\mu_u \frac{\partial u_j}{\partial x_i} + \mu_u \frac{\partial u_i}{\partial x_j}\right) - \rho U \frac{\partial u_j}{\partial x_i} \qquad (2)$$

ρ-density, p-pressure, U-welding velocity, μ_u-Non-Newtonian viscosity.

Viscosity is equal to the flow stress divided by the effective strain rate [Nandan et. al. 2007]:

$$\mu_u = \frac{\sigma_f}{3\dot{\varepsilon}} \qquad (3)$$

Maximum stresses are usually determined from a hyperbolic-sine constitutive relationship with coefficients determined from experimental tests such as hot tension, hot compression or hot torsion tests for a wide range of temperatures and strain rates. The flow stress (perfectly plastic model) proposed by Sheppard and Wright [in Nandan et. al. 2006] is:

$$\sigma_f = \frac{1}{\alpha} sinh^{-1}\left[\left(\frac{Z}{Ai}\right)^{\frac{1}{n}}\right] \qquad (4)$$

Where n, Ai, α are material constants.

A previous work on C-Mn steel showed that the parameter A_i can be written as a function of carbon percentage as follows [Nandan et. al. 2007]:

A_i=1.8 x10^6 +1.74 x10^8 (%C)- 6.5 x 10^8 (%C)^2 (5)

α and n are temperature dependents and can be represented as:

α=1.07+1.7 x10^{-4} T-2.81 x10^{-7} T^2 (6)

n=0.2+3.966 x10^{-4}T (7)

Z_n is the Zener-Holloman parameter representing the temperature compensated effective strain rate [Nandan et. al. 2006]:

$$\mathrm{Zn} = \dot{\varepsilon} \exp\left(\frac{Qe}{RT}\right) = Ai[\sinh \alpha \sigma_f\ )]^n \quad (8)$$

$$\mathrm{Zn} = \dot{\varepsilon} \exp\left(\frac{Qe}{RT}\right) = Ai \exp(\alpha n \sigma) \quad (9)$$

Qe is the activation energy. The effective strain rate can be represented as:

$$\dot{\varepsilon} = \sqrt{\frac{2}{3}\varepsilon_{ij}\varepsilon_{ij}} \quad (10)$$

ε_{ij}- is the strain tensor which can be represented as:

$$\varepsilon_{ij} = \frac{1}{2}\left(\frac{\partial u_j}{\partial x_i} + \frac{\partial u_i}{\partial x_j}\right) \quad (11)$$

Heat equations for a moving heat source:

FSW tool is represented as solid whereas the workpiece material is represented as liquid in the Eulerian framework which flows through the mesh usually in steady state solution [Schmidt and Hattel 2005]:

$$\rho C_p \nabla(uT) = \nabla(k \nabla T) - \rho C_p v_x \frac{\partial T}{\partial x} + Q_i + Q_b \quad (12)$$

v_x :Velocity in the X:direction, T: Temperature, Q_i : Heat generated due to tool/workpiece interface, Q_b : Heat generated due to plastic deformation away from the interface.

Heat flux (q) between the tool/workpiece interfaces was derived from Q_i as [Schmidt and Hattel 2005]:

$$q = \omega r \tau_{contact} \quad (13)$$

To relate the velocity of a point at the interface to the tool velocity a new parameter is defined to describe the contact condition. The contact condition can be either sliding without deformation of workpiece or sticking with deformation of workpiece or partial sticking/sliding [Schmidt et al 2004]. The following equations (14 and 15) show two of such conditions.

$\tau_{contact} = \tau_y$ Sticking (representing the plastic deformation) (14)

$\tau_{contact} = P\mu$ Sliding (representing the frictional force per unite area) (15)

μ: Friction coefficient, P: Tool pressure (in Pa). $\tau_{contact}$: Contact shear stress (in Pa) ω: Tool rotational speed (RPM) and r is the Tool Radius (mm). τ_y :is the Yield shear stress (in Pa) and is a function of

temperature. The yield shear stress is representing the heat generated from plastic deformation when multiplied by ωr and generally is calculated with the relationship of yield stress as follows [Nandan et. al. 2007]:

$$\tau_y = \frac{\sigma_y}{\sqrt{3}} \quad (16)$$

σ_y is the yield stress. Generally steel starts to yield when the temperature exceeds 650 K and its value almost vanishes when the temperature exceeds 1100K [Nandan et. al. 2007]. Figure 3 shows the variation of yield stress with temperature for mild steel [Nandan et. al. 2007].

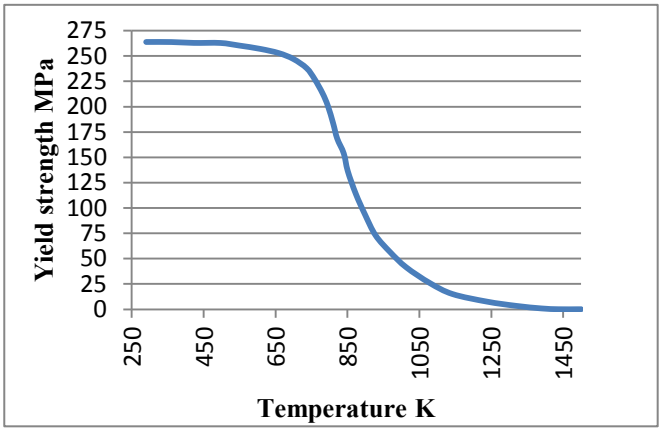

Figure 3: The variation of yield stress with temperature for mild steel [Figure adopted from Nandan et. al. 2007 P885].

$P\mu$ -is the frictional force per unite area that when multiplied by ωr represents the rate of frictional heat per unit area. Contact condition can become partial sliding/sticking if, at low strain rate which is not sufficient for fully sticking condition, the contact shear stress exceeds the yield stress. So for sticking/sliding conditions the heat flux can be represented as follows [Schmidt et. al. 2005]:

$$q = [(1-\delta)\tau_y \eta + \delta\mu P](\omega r - U\, sin\theta) \quad (17)$$

where U is the velocity of the tool in the welding direction (m/s), η the amount of mechanical energy converted to heat energy (machine efficiency), θ rotation angle of the tool. The term $U \sin\theta$ represented a small value in heat generation contribution so it was ignored.

r is the radial distance of the centre of the area from the tool axis, ω is angular velocity and δ is the sticking/sliding parameter (0 sticking, 1 sliding), which has been established and improved previously by matching the measured values at various relative velocities [Nandan et. al. 2008]:

$$\delta = 0.2 + 0.8 * \left\{1 - \exp\left(-\frac{\omega r}{\omega_o \delta_o R_o}\right)\right\} \quad (18)$$

Where R_o is the radius at tool periphery, ω_o is the maximum rotational speed of the tool (RPM), δ_0 is a constant and ω is the local rotational speed in the contact region. ω can be expressed as:

$$\omega = \frac{\omega_o r}{R_o} \quad (19)$$

The values of friction coefficient, μ, can be estimated from the relative velocity in the contact region between the tool and plate; in this work μ has been estimated from a previous work carried out on FSW of steel [Nandan et. al. 2007]. Relative velocity values vary from ωR_s at the outer edge of the tool shoulder to zero at the axis of rotation.

Figure 4 shows the variation of δ based of the tool radius. In the current work, the initial value which fulfils a suitable fitting of the curve was taken as $\delta_o = 0.2$. The data points of the curve were calculated using previous experimental work conducted on rolling of steel as follows [Deng et. al. 2001]:

$$\mu = \mu_o \exp(-\delta \omega r) \qquad (20)$$

Where μ_o : is the initial friction coefficient and can be estimated experimentally from the welding charts, here the initial value was taken as $\mu_o = 0.3$. Figure 5 shows the variation of friction coefficient with the tool radius in which a significant drop is observed in its value at the tool periphery when the rotational speed increases.

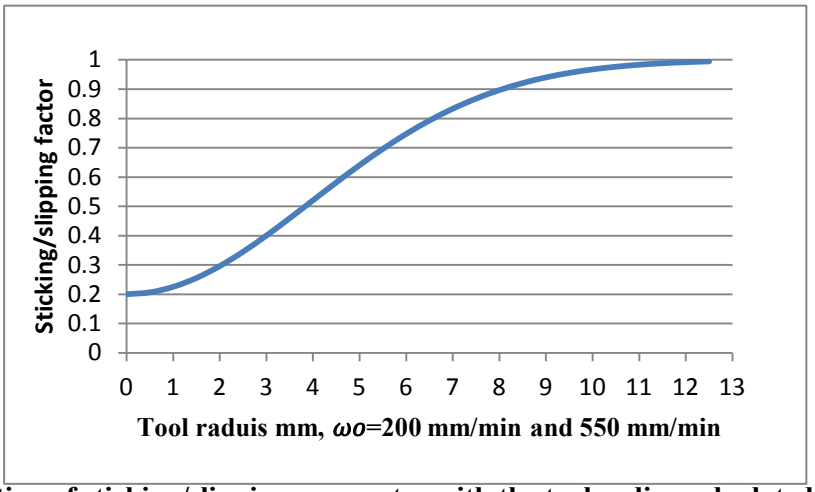

Figure 4: Variation of sticking/slipping parameter with the tool radius calculated from eq. 20.

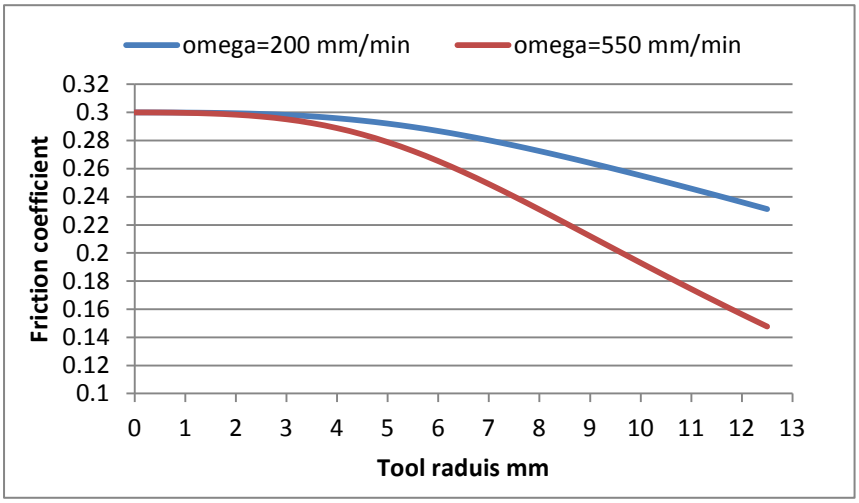

Figure 5: Variation of coefficient of friction with the tool radius. The value of friction coefficient decrease significantly at the tool periphery when rotational speed increases.

Heat generated due to plastic deformation (Q_b)

Under the effects of viscous dissipation some heat can be produced by plastic deformation experienced by the material adjacent to the tool periphery; this heat can be calculated as [Arora et.al. 2009, Nandan et. al. 2007]:

$$Q_b = \varphi \mu_u \aleph \quad (21)$$

$$\aleph = 2\sum_{i=1}^{3}\left(\frac{\partial u_i}{\partial x_i}\right)^2 + \left(\frac{\partial u_1}{\partial x_2} + \frac{\partial u_2}{\partial x_1}\right)^2 + \left(\frac{\partial u_1}{\partial x_3} + \frac{\partial u_3}{\partial x_1}\right)^2 + \left(\frac{\partial u_3}{\partial x_2} + \frac{\partial u_2}{\partial x_3}\right)^2 \quad (22)$$

Where $\mu_u \aleph$ is the heat generated in fluids which has much lower viscosity (W), μ_u is Non-Newtonian viscosity (Pa.s), φ isa constant (with the value of 0 to 1 , with 1 representing a well-mixed system) and usually used to reduce the heat generation and to make it suitable with the context of high-viscosity plasticized materials, the value used was 0.05 [Nandan et. al. 2007].

Boundary Conditions

A- Representing the Material Flow:

The coordinate of a specified node in the contact region is shown in Figure 6; as the tool moves and rotates the node is transferred from location 1 to 2 and can be represented as [Darvazi et. al. 2014]:

$$X = U\,t + r(\cos(\theta) - \cos(\theta_o)) \quad (23)$$

$$Y = r(sin(\theta) - \sin(\theta_o)) \quad (24)$$

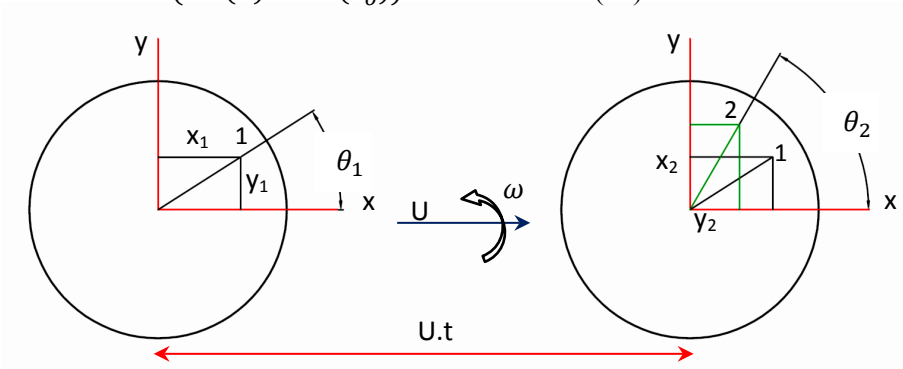

Fig 6: Material flow around the tool in FSW [Figure adopted from Darvazi 2014 P1303].

By deriving these coordinates equations, and representing the sticking/sliding parameter, the velocities (u,v) in x and y directions can be obtained as:

$$u = (1-\delta)(\omega r\, sin\theta - U) \quad (25)$$

$$v = (1-\delta)(\omega r\, cos\theta) \quad (26)$$

Velocity in the x-direction was represented to compensate for the thread effect in the actual tool geometry as following [Darvazi et. al. 2014]:

$$w = \gamma \frac{R_p \omega}{2\pi} \quad (27)$$

γ, R_p are the pitch and radius of the pin respectively.

B-Heat Fraction between the Tool and the Workpiece:

Due to the low thermal conductivity of DH36 steel (as received from the manufacturer =45-55 W/m. ^{o}C) compared to the tool (PCBN) which is about four times that of steel, most of the heat generated in the FSW process will be partitioned between the tool and work piece.

Other researchers [Darvazi et. al. 2014, Nandan et. al. 2007] calculated this fraction (f) as : $f = \frac{J_{WP}}{J_{WP}+J_{TL}} = \frac{\sqrt{(k\rho C_p)_{WP}}}{(k\rho C_p)_{WP}+(k\rho C_p)_{TL}}$ (28)

$$q = h(T - T_\circ) + \epsilon\sigma(T^4 - T_\circ^4) \quad (29)$$

where f is heat fraction between the tool and workpiece, ϵ emissivity of the plate surface, β is Stefan-Boltzmann constant (5.670373×10^{-8} W m^{-2} K^{-4}), T_o initial temperature (^{o}C), h heat transfer coefficient (W/m^2.^{o}C) and the abbreviation wp and TL refer to the workpiece and the tool, respectively.

The heat fraction transferred to the workpiece was estimated to be between 0.4-0.45 for welding using a tungsten based tool and workpieces of mild or stainless steel 304L [Darvazi et. al. 2014]. However, for FSW using PCBN tool with a cooling system as in this work, the equation cannot accurately represent the heat fraction between tool and workpiece because the PCBN tool is a hybrid tool which includes four types of materials with different thermal properties. The presence of the cooling system and gas shielding will influence the heat partitioning. Subrata and Phaniraj 2015 showed that equation 28 is only valid when the tool and plate are considered as an infinite heat sink with no effects of heat flow from air boundary of the tool. They found that the heat partitioned to the tool is less than that calculated from equation 28.

C-Heat Losses from Workpiece Surfaces (Top and Side walls)

Convection and radiation in heat transfer are responsible for heat loss (Q) to the surroundings and can be represented as:

$$Q = hA(T - T_o) + \varepsilon\beta A(T^4 - T_o^4) \quad (30)$$ And

$$k\frac{\partial T}{\partial n}\Big]_\Gamma = q = h(T - T_o) + \varepsilon\beta(T^4 - T_o^4) \quad (31)$$

T_o is the ambient temperature (25^{o}C), n is the normal direction of boundary Γ.

In the current model, radiation is not be calculated as it adds more complexity to the case. Instead the value of heat convection coefficient around the tool was increased. [Micallef et. al. 2015].

D-Heat loss from Workpiece Bottom Surface

The bottom of the workpiece was in direct contact with two other plates (usually mild and O_1 steel grades) and the anvil. Previous workers [Khandkar et. al. 2003, Micallef et. al. 2015] have suggested to represent the backing plates effects by a convection heat condition with a higher coefficient of heat transfer values (500-2000 W/m^2. ^{o}C). However, the exact value of the heat coefficient applied to the bottom surface is not accurately known and the data related for this simulation is limited. Hence, a value of 2000 W/m^2. ^{o}C was used which gave a good agreement of temperature distribution with the previous work [Toumis et. al. 2014 (c)].

The initial temperature of the workpiece was set at room temperature (25^{o}C) and all governing equations and boundary conditions were carried out in Fluent software research version which is able to solve the 3D equations of velocity and momentum.

Mechanical and Metallurgical examinations: Tensile, Fatigue, Infinite Focus Microscopy (IFM) and Scanning Electron Microscopy (SEM) examinations were carried out to check the weld quality and estimate the defects and phase changes after the FSW process.

Plate preparation (DH36 Steel) for tensile and fatigue tests:
All test materials were taken from the steady state region of FS welded sections. The plates were water-jet cut to minimise any mechanical damage. The tensile test samples were taken from the steady state region according to the British Standard of EN-BS 895:1995. Eight samples were tested, (2 samples from the parent metal were taken in the direction of rolling for better estimation of tensile parameters and 6 samples from the steady state welded zone in a normal direction to the welding). These tensile samples were tested at the test facility at Zwick/Roell Company in Germany. The test was conducted using Schindler Z250 at test speed of B, with a pre-load of 2 MPa and test speed of 0.0067 1/s . Six samples taken from each plate were prepared for the Fatigue test based on BS 7270 standard. The sides of samples were polished in the longitudinal direction to reduce the effects of any sharp edges that could cause crack propagation. The load set of 0.8 of the yield stress maximum of 305.6MPa and minimum of 30.56 MPa, mean stress=168.1MPa and amplitude=137.5MPa were used [Toumpis et. al. 2015]. Stress frequency was kept constant at 10Hz during the testing program. The sample dimension for fatigue and tensile testing are shown in Figure 7.

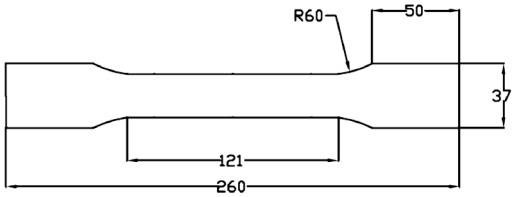

Figure 7: The dimensions of Tensile and Fatigue sample (in mm) conducted based on EN-BS 895:1995 and BS 7270 standards

SEM Images:
Scanning Electron Microscopy examination was carried out on the polished and etched (2%
Nital) FSW samples including the surface of SZ and also parent metal. The SEM produced high resolution images of micro constituents by employing secondary electron (SE) imaging mode with accelerated voltage of 20 kV. The working distance (WD) used was 5 mm but in some cases altered (decreased or increased) to enhance the contrast at high magnification. The main aim for this microstructural assessment was to gather information about the phases that were likely to be present in the weld zone and to use that information to understand and predict mechanical properties of the joints. It was also to gather information related to undesirable process-induced defects or flaws that could compromise the integrity of the joint.

Infinite Focus Microscopy (IFM): IFM was used to calculate the exact area for the PCBN tool to enhance the accuracy of the calculations needed for modelling. The technique was also applied on FSW samples to obtain macrograph of SZ and HAZ. This was done by scanning the areas of interest and transferring them into a 3-D image, and then calculating the surface area by the aid of Lyceum software.
Two welding conditions were used in the analyses which are given in Table 3:

Table 3: FSW conditions of low and high welding speeds of DH36 steel.

Weld No.	Rotational speed RPM	Traverse speed mm/min	Rotational/ Traverse	Torque N.m	Axial force (average) KN	lateral force (average) KN	exp(-lateral force/axial force)
W1	200	100	2	278 average	57.55	12.8	0.8
W2	550	400	1.375	200-325	67.1	13.4	0.2

Results and Discussion: In all the following figures (Fig. 8- Fig. 13) the advancing side is on the right hand side on the image

Temperature Distribution in the Tool and Workpiece

Figure 8 shows temperature distribution in the advancing side of the top surface of the plates in which -a- and -b- are for slow (W1) and high welding speed (W2), respectively. The contours of temperatures of both low and high welding speeds (as shown in Figure 8) are compressed in front of the tool but expanded behind it. This is in fact the effect of material moving from the inlet to the outlet while the tool is rotating, generating a plastic/frictional heating. The contours are also more compressed in the high travelling speed compared to the low travelling speed and this certainly leads to a higher cooling rate. Figure 9 illustrates the temperature contour distribution between the advancing and retreating sides for both slow (a) and high welding speed (b). It shows that the HAZ for slow welding speed is larger than that for high welding speed. This means that steel around the tool experienced a temperature rise for a longer time in slow travelling speed than in high travelling speed. In agreement with this finding, Micallef et. al. 2015 also showed a similar effect of welding speed on the HAZ of the same thickness and same grade of steel plate.

In the current model, for slow welding speed a peak temperature of 1010^{o}C has been estimated with a nearly symmetrical distribution between advancing side (AS) and retreating side (RS) (Fig. 9-a), while for high welding speed (Fig. 9-b-), a maximum peak temperature of 1250^{o}C with asymmetric distribution between AS and RS is predicted. In both cases the maximum peak temperature was found in the advancing-trailing side as results of high relative velocity which cause a maximum flow value of material in that location. Fehrenbacher et. al. 2014 measured a maximum temperature in the advancing-trailing side of a sample of aluminium alloys using thermocouples. Micallef et. al. 2015 confirmed from CFD modelling that the maximum temperature occurred in the advancing side but near the trailing side. Darvazi et. al. 2014 also showed by CFD that maximum temperature of FSW of stainless steel 304L was in the back of the shoulder towards the advancing side. The maximum peak temperature in the current model was compared with previous works done on the same thickness and grades of steel [Toumis et. al. 2014 (c), Micallef et. al. 2015] and it is found to be in agreement with their results; however, the asymmetry between advancing and retreating sides is clearer in the current model than in previous works.

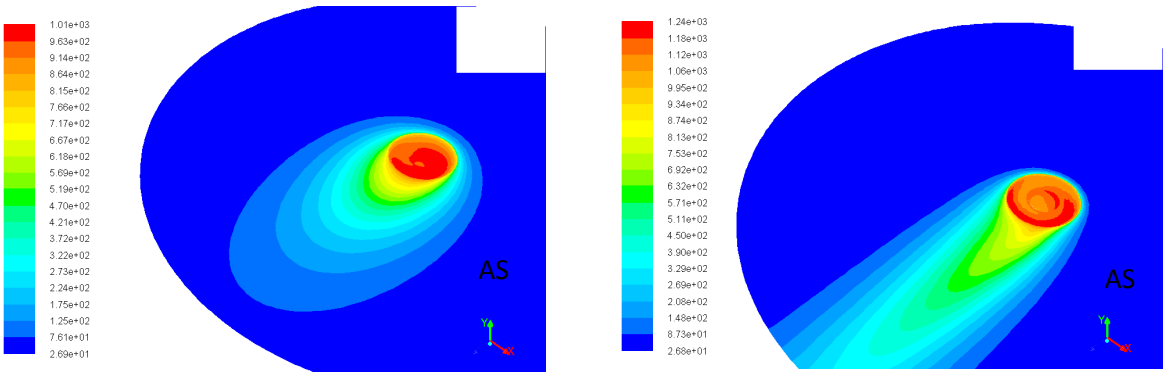

-a- **-b-**

Figure 8: Temperature distribution in the top surface of plate a- slow speed weld (W1), b- high speed weld (W2), Note AS stands for Advancing Side..

As shown in Figure 9, the heat transfer to the tool is through conduction; this can be seen from the contours' shape which bends towards the tool shank. As the thermal conductivity of the tool collar is very low, it acts as an insulator, so most of the heat generated will partition between the PCBN tool and shank from one side and the workpiece from the other side.

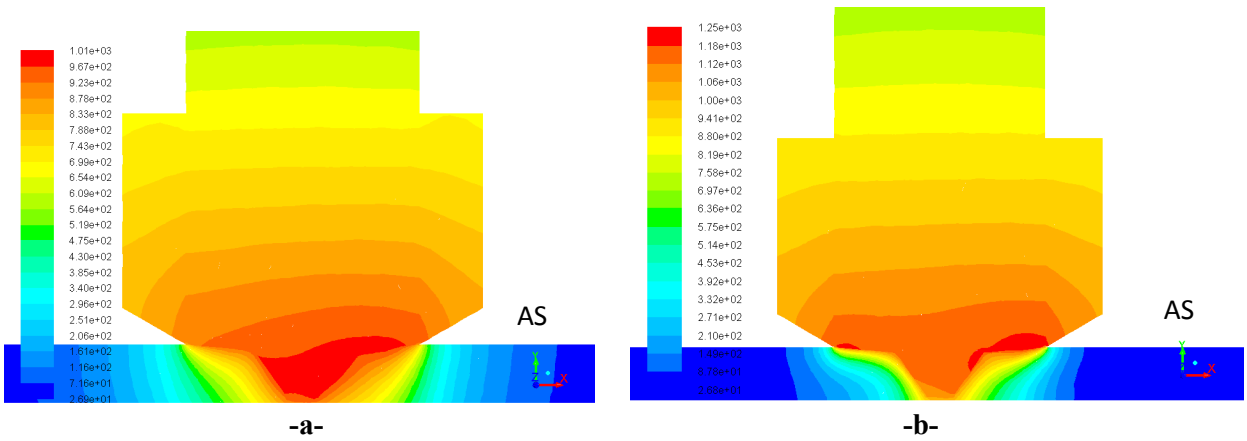

Figure 9: Temperature contour distribution between the advancing and retreating sides. a- slow speed weld (W1), b- high speed weld (W2).

Figure 10 illustrates the temperature distribution around the tool surfaces for two different welding speeds (slow: W1, and high W2).

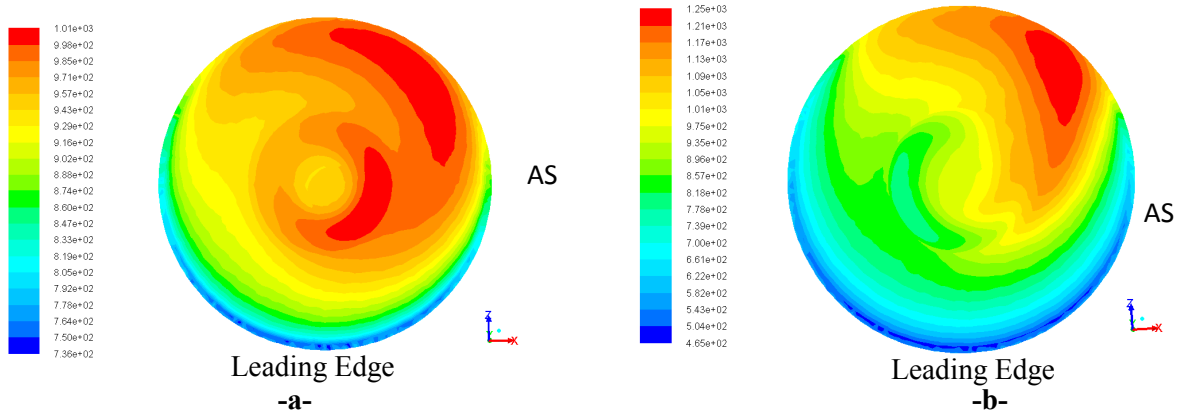

Figure 10: Temperature distribution around the tool. a- slow speed weld (W1), b- high speed weld (W2).

As shown from Figure 10, the FSW tool surface experiences different temperatures during the welding process. The front direction (leading edge) experiences lower temperature than the back direction (trailing edge). This temperature difference is because the material in contact with the leading edge is experiencing lower plastic deformation compared to the trailing side as the material being pushed behind the tool towards the advancing-trailing side. Temperature difference is increased with increasing the travelling speed as shown in Fig. 10 -b. This can cause an increase in shear forces on the tool surface especially on the leading edge. Micallef et. al. 2015 and Elbanhawy et. al. 2013 also reported the same differences in temperature distribution around the tool surfaces.

Strain rate and material flow: Figure 11 shows the strain rate distribution in the tool/ workpiece contact region for two different welding speeds (slow: W1 and high: W2) at the advancing side. It illustrates that strain rate reaches its maximum values at the contact zone between the tool and workpiece where the peak value is just under the tool shoulder. The slow welding speed gave a maximum strain rate of 153 s^{-1} whereas the high welding speed showed an increase in the strain rate with the maximum value of 337 s^{-1}, this was due to the increase in relative velocity of the adjacent welded material. Such increase in strain rate with an increase in the tool's speed was also reported by

Fairchild et. al. 2009. The value of strain rate decreases towards the probe end due to the lack of material flow in this region resulted from a decrease in relative velocity.

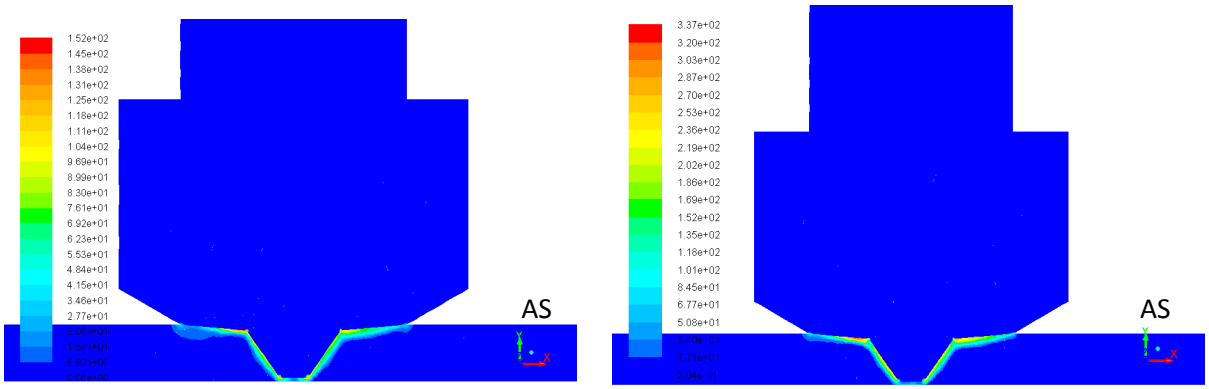

Figure 11: Strain rate distribution in the tool/workpiece contact region. a- slow speed weld (W1), b- high speed weld (W2).

Figure 12 shows the material flow (maximum relative velocity) around the tool for two different welding speeds (slow: W1, and high: W2) at the advancing side. It shows that the maximum relative velocity of the slow welding speed was 0.08 m/s while in higher welding speed it was 0.219 m/s. It is worth noting that material flow around the tool is almost symmetrical at the slow welding speed due to low travelling speed so the formation of stagnant zone is limited. However, with increasing travelling speed (high welding speed shown in Fig. 12-b) the flow is asymmetrical and a stagnant zone was formed in the advancing-trailing side where the flow was deflected at the retreating side in the direction of rotation. The formation of this stagnant zone can result in defects such as wormhole and voids at this region.

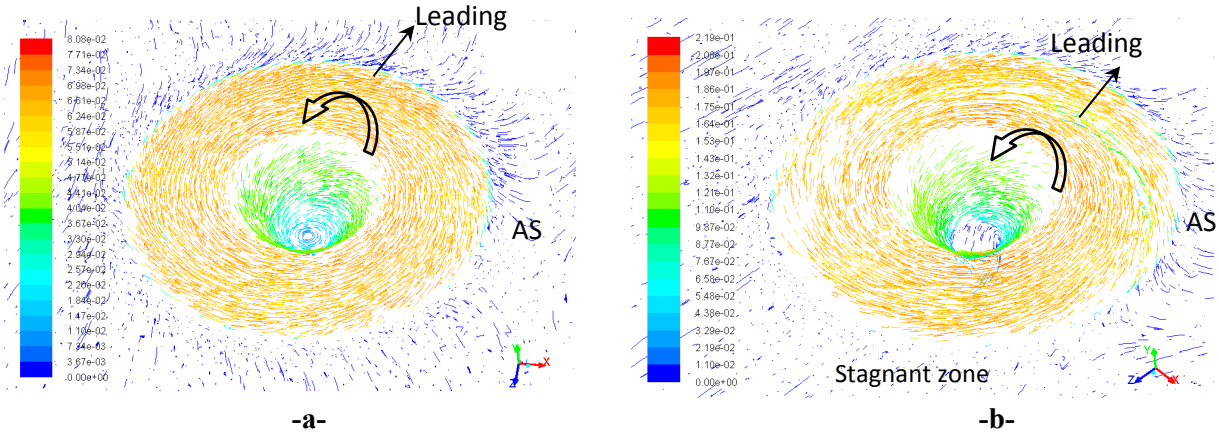

Figure 12: Material flow around the tool (in term of maximum relative velocity), a- W1 slow speed weld, b- W2 high speed weld.

Schmidt et. al. 2006 carried out some experimental works on aluminium to study the material flow around the FSW tool; they showed the same trend for the material flow as found in this work;, where marker foils of copper flowed around the tool, broken into pieces then they reverted around the retreating side in the same direction of rotation. Morisada et. al. 2014 used a W tracer with the aid of XR transmission system to monitor the material flow during FSW of low carbon steel and found that the shape of the stirred zone in steel is changed because of the formation of a stagnant zone at the

advancing side. Due to the relatively high deformation resistance behaviour of steel, they suggested low rotational speed would produce a uniform flow zone with optimal FSW conditions. It is also shown from Fig. 12 that a shear layer was formed around the tool contact region; this means that this region experienced plastic deformation, a high strain rate, high temperature and thus low viscosity and can be a part of the SZ and together with the main stirred zone can form the final shape of the thermo-mechanical affected zone (TMAZ). It is worth noting that size of the shear layer increases with increasing tool rotational speed.

The importance of material flow as a main source of heating in the FSW process can be determined by Peclet (P_e) number which is the heat transfer by convection to that by conduction and is calculated from the following equation [Nandan et. al. 2007]:

$$\mathrm{Pe} = \frac{\rho\, U_c\, C_p\, L_c}{k} \qquad (32)$$

where U_c is the characteristic velocity and equals to 0.219 m/s for the high welding speed (see Figure 12), and L_c is the characteristic length which represents the shear layer thickness taken from IFM experiment (on average 0.0125m).

So in this work, Pe will be equal to 221 which indicate that material flow plays a major role in heat transfer during FSW process of steel especially under the tool shoulder. The importance of material flow in heat transfer during FSW process was also reported by Grujicic et. al. 2010 and Nandan et. al. 2006 for modelling aluminium AA5083-H131 where they found that Pe number was still high even when the thermal conductivity is very high.

Viscosity variation around the tool:

Figure 13 presents the spatial variation of viscosity around the tool for two different welding speeds (slow: W02, and high: W52) at the advancing side.

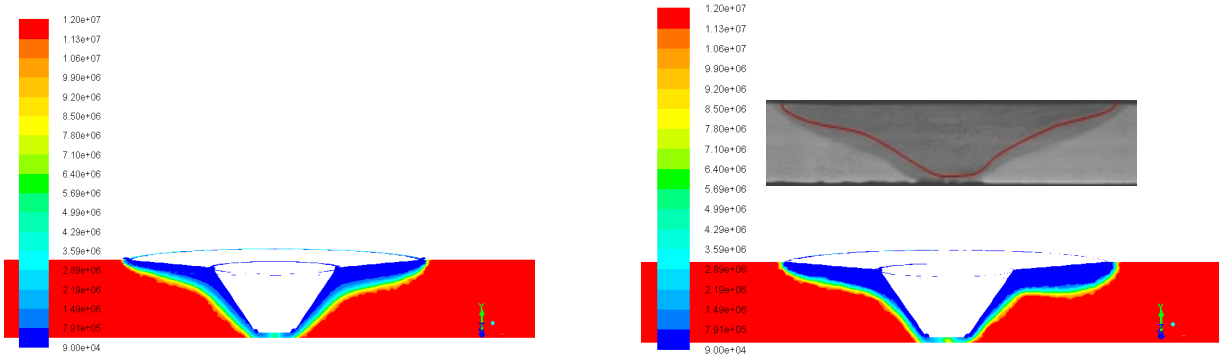

-a- **-b-**

Figure 13: The spatial variation of viscosity a- W1 slow speed weld, b- W2 high speed weld.

The viscosity variation around the tool as shown in Fig. 13 defines the shape of the SZ. The value of viscosity in both low and high welding speeds shows a significant decrease around the tool shoulder and probe side but less towards the probe end. This variation is due to the mechanical combination of both shoulder and probe side in the top surface of the workpiece which results in high strain rate and an associated temperature increase and in turn leads to a decrease in the viscosity as viscosity is inversely proportional to strain rate and temperature. The decrease in viscosity around the tool encourages the layers of steel adjacent to the tool to rotate with a high velocity in the top of the SZ but less in the bottom of the plate. The high values of viscosity in areas just after the rotated layers will make the material flow more difficult. This defines the limits of SZ which forms a V-shaped geometry

around the contact region. The same viscosity behaviour around the tool was reported by Nandan et. al. 2007 for FSW of mild steel. Figure 13 shows that the material can flow in a viscosity ranged from 0.09×10^6 to 9.8×10^6 Pa.s which is in agreement with a previous work conducted on mild steel by Nandan et. al. 2007. From the viscosity, strain rate, velocity and temperature contours (given in Figures 8 to 13) it can be inferred that the tool shoulder and probe side play the most important part in generating the heat required for welding, and the probe end does not play a major role in stirring the material in the contact region.

Torque in the contact region: The torque is calculated under the shoulder of the tool as it represents the major part of the total torque [Zhang and Zhang 2014] and is coming mainly from the viscous and local pressure forces as follows:

$$M = F_p \times r + F_v \times r \qquad (33)$$

where M, F_p, F_v, and r are the torque (N.m), pressure force (N), ,viscose force (N), and distance from the torque centre to the force origin, respectively.

From the CFD model, the calculated torque for low and high welding speeds were 269 and 230 N.m, respectively which is within the range of experimental torque values calculated by the FSW machine (outlined in Table 3). The torque results give confidence in the assumptions used in the CFD modelling in this work.

Tensile and fatigue test results

Figure 14 shows photographs of the failed tensile test pieces. It shows that all the tensile samples failed outside the welding region; this means that any welding defects did not affects the strength of SZ. 0.2% proof stress was 475 MPa for the parent metal (which is in accord with the manufacturer's data (473MPa) [Masteel 2015] whereas for the FSW samples it was slightly higher and this higher value for proof stress for welded condition was also reported by Reynolds et al 2003. In this work, the average ultimate strength of the welded samples was 580 MPa. Similarly Cater et. al. 2013 reported a tensile strength of 570 MPa for the same grade of steel which is slightly lower than the findings of the current work. The increase in tensile strength of the FSW samples is attributed to the refinement of microstructure which will be discussed in the SEM results section. Figure 15 shows the fatigue test specimens for two different FSW samples, (a) W1 low speed and (b) W2 high speed conditions.

Fig. 14: Photographs of tensile testing samples, the broken FSW sample and also a sample for parent metal.

-a- W1 -b- W2

Fig. 15: Fatigue test of a-high speed welding and b-low speed welding.

Figure 15 a shows a fatigue specimen welded with a high welding speed ; this sample failed in the welding zone of an average of 111,736 cycles and the crack initiated from the back middle of the plate towards the advancing side. This could be associated with defects (cracks) found in the SZ (this will be discussed in the SEM section below). However, for the slow welding speed sample (shown in Fig. 15 –b) if failed just outside the SZ in the advancing side and survived up to 644128 cycles. The high strength for fatigue in the low welding speed samples is attributed to its defect free and fine microstructure formed in SZ during FSW process (this will be shown in the SEM section).

Microstructure Evolution

Figure 16 shows the microstructure of the parent metal which consists of ferrite and pearlite bands. Figure 17 and 18 reveal SEM micrographs of SZ for samples welded at high and low welding speeds, respectively. Figure 16 shows that the material has experienced a phase transformation following FSW; this indicates that the welding temperature was above the A_3 line of Fe-C equilibrium phase diagram. The advancing side of the high speed weld W2, (Fig. 17-a) shows a different microstructure from the retreating side. A mixed microstructure of acicular ferrite and recrystallized ferrite grains of 2μm decorated by cementite is found at the advancing side (as shown in Figure 17–a); this microstructure is expected to have experienced a high temperature range, high strain rate and slower cooling rate [Samuels 1999]. The microstructure of the retreating side (Figure 17-b) shows a mix of bianite and acicular ferrite which is usually formed at a higher cooling rate, so it is expected the retreating side has experienced a lower temperature than the advancing side. Darvazi et. al. 2014 reported that asymmetry in temperature is dominant under the shoulder more than other regions. In this work, the microstructure at low welding speed shows a combination of acicular ferrite and bainitic ferrite which was symmetrical between advancing and retreating sides as shown in Figure 18.

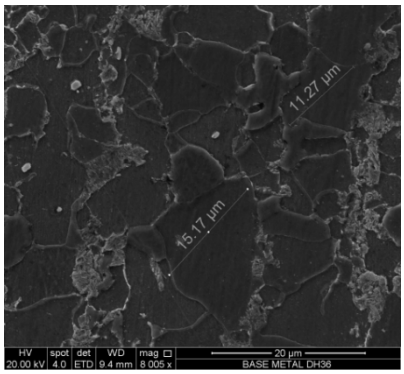

Figure 16: The microstructure of base metal consisting of ferrite and bands of pearlite.

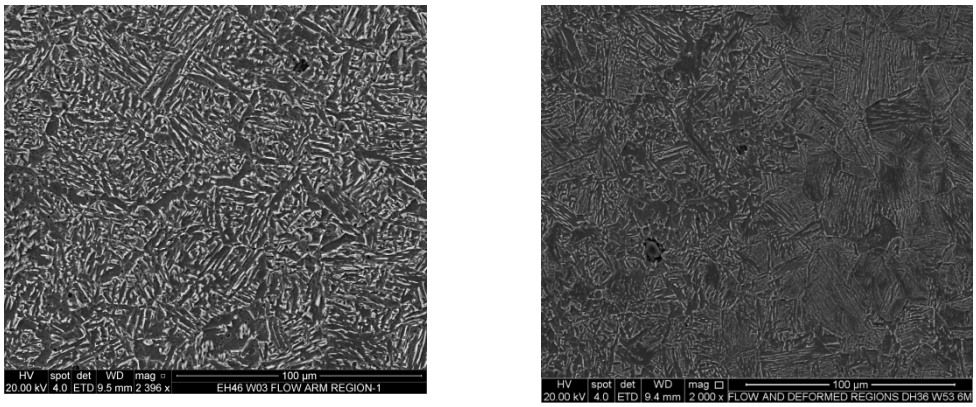

-a- **-b-**

Figure 17: SEM microstructure of SZ region of FS welded sample at high welding speed W2 (-a- advancing side at the tool periphery showing a combination of acicular ferrite and ferrite grains of 2µm size decorated by cementite. -b-: micrographs of the retreating side showing a mixture of bainite and acicular ferrite.

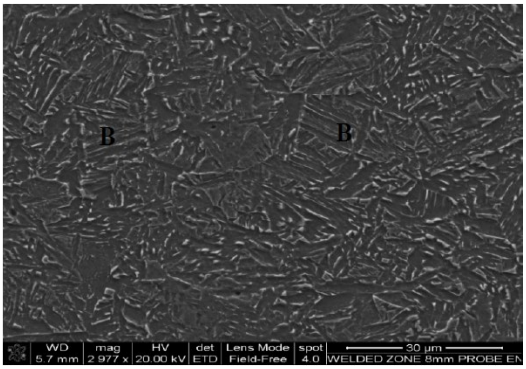

Figure 18: SEM microstructure of SZ region of FS welded sample at low welding speed (W1) showing a combination of bianite and acicular ferrite.

Welds defects

Samples welded at low welding speed did not show any visible defects; however, samples welded with high welding speed showed some defects. Figure 19 illustrates a macrograph of the steady state region FS welded at high welding speed. Macro cracks (as shown in Figure 19) were found in the SZ of sample treated at high welding speed. The first macro crack appears from the bottom of the plate with a length of 2 mm towards the SZ but near the advancing side. These types of defects were investigated previously by other researchers [Stevenson et. al. 2015] where they were identified as weld root flaws and as attributed to an insufficient tool plunge depth or a deviation of the tool from the centreline. As this type of defect is found along all the weld line, it is unlikely that the tool deviation was the main cause for the defect here. This macro crack may be due to the lack of velocity and strain rate under the probe end which causes a stagnant zone to be formed and leads to a lack of plasticity as seen in the CFD model. The material in this region will be vulnerable to crack formation under the normal plunge force, so any uneven surface or sharp edge will act as a stress concentration point. In addition, insufficient penetration of the tool caused the material underneath to remain un bonded and as a result a crack will be observed. Figure 20 shows SEM micrographs of the first and second cracks presented in Figure 19. For the future works, more investigation about this type of defect and its relation to applied forces is recommended.

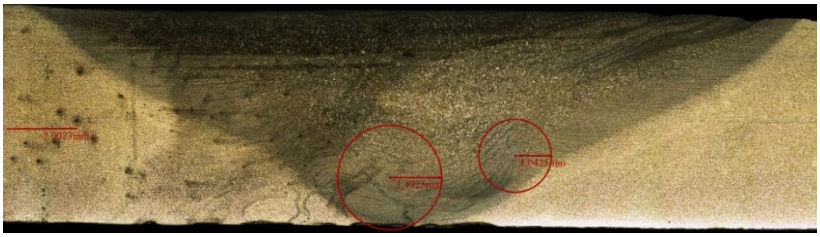

Figure 19: Macrographs of the steady state region of high welding speed (W2).

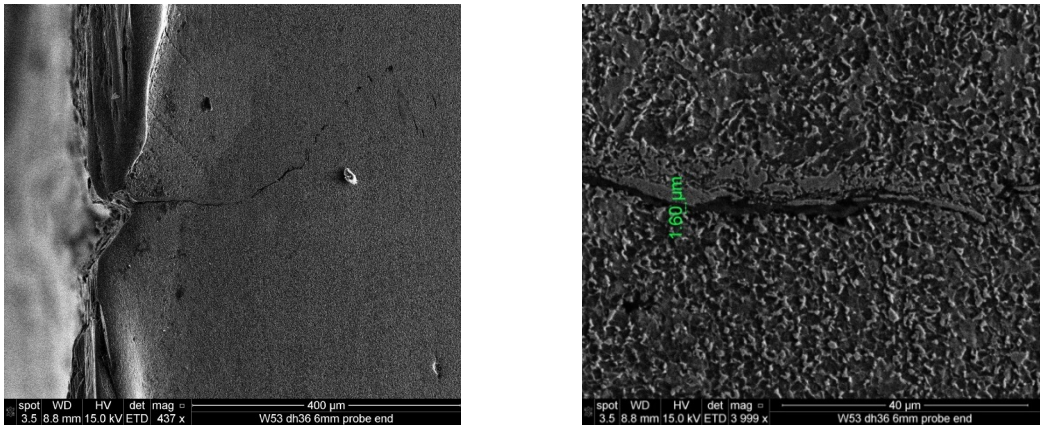

-a- **-b-**

Figure 20: SEM of the first and second cracks shown in Fig. 4 -a- under and around the probe.

Conclusions:

A CFD model developed here represented the heat generated, asymmetry, strain rate and material flow during FSW process of DH36 steel grade. Its success has been confirmed by some prior experimental values as well as some readings from the FSW machine. The following findings are concluded for their work.

-The tool shoulder and probe side were found to be the main sources of heat generated during FSW. The V-shape of SZ was found to be the result of the mechanical combination of these two parts.

-The peak temperature under the tool region increased with increasing rotational speed; however, the cooling rate was also increased with increasing travelling speed. This explains the increase in the asymmetry in the microstructure between the Advancing and retreating sides of high welding speeds.

-Defects were found in the microstructure when the tool travel speed was increased. This was found to be due to the lack of material flow (stagnant zone formation) especially on the advancing side.

-The microstructure of the base metal has been improved after the FSW process and showed a refinement and phase transformation from ferrite and pearlite bands to bainite and acicular ferrite.

- High welding speed weakened the fatigue resistance which was attributed to the formation of defects.

-The tool was exposed to different temperature distribution during FSW process. Higher temperature was observed at the advancing-trailing side and lower at the leading side.

Acknowledgement

The Authors would like to thank Mr Thomas Alan from Zwick/Roll for his help in performing the mechanical testing. The Authors also thank TWI company for providing samples and data.

References

Arora A., Nandan R., Reynold A.P. and DebRoya T., 2009, Torque, power requirement and stir zone geometry in friction stir welding through modelling and experiments. Scripta Materialia, 60(1), pp.13–16.

Atharifar H., Lin D., and Kovacevic R ,2009, Numerical and Experimental Investigations on the Loads Carried by the Tool During Friction Stir Welding, Journal of Materials Engineering and Performance, Volume 18(4), pp. 339-350.

Barnes S.J. , Bhatti A.R., Steuwer A., Johson R., ALTenkirch J. and Withers P.J., 2012. Friction Stir Welding in HSLA-65 Steel: Part I. Influence of Weld Speed and Tool Material on Microstructural Development. Metallurgical and Materials Transactions A, 43(7), pp.2342–2355.

Cater S., Martin J., Galloway A., McPherson, 2013, Comparison between friction stir and submereged arc welding applied to joining DH36 and E36 shipbiulding steel, Friction stir welding proceeding VII, pp.49-58.

Cui, L., Hidetoshi F., Nobuhiro T., Kazuhiro N., Kiyoshi N., Rinsei I and Muneo M., 2007. Transformation in Stir Zone of Friction Stir Welded Carbon Steels with different carbon content, ISIJ International , 47(2), pp.299–306.

Darvazi, A.R. & Iranmanesh, M., 2014, Thermal modeling of friction stir welding of stainless steel 304L. The International Journal of Advanced Manufacturing Technology,75 (9-12), pp.1299–1307.

Deng, Z., Lovell, M.R. & Tagavi, K. a., 2001. Influence of Material Properties and Forming Velocity on the Interfacial Slip Characteristics of Cross Wedge Rolling. Journal of Manufacturing Science and Engineering, 123(4), p.p. 647-653.

Elbanhawy A., Chevallier E., Domin K., 2013, Numerical investigation of friction stir welding of high temperature materials, NAFEMS world congress, Salzburg, Austria, 9-12 June 2013.

Endo R., Shima, M., Susa, M. ,2010, Thermal-Conductivity Measurements and Predictions for Ni–Cr Solid Solution Alloys, Int J Thermophys , 31:1991–2003.

Fairchild D. , Kumar A. , Ford S. , Nissley N., 2009, Research concerning the friction stir welding of linepipe steels, Trends in welding research, Proceedings of the 8th International Conference, pp.371-380.

Fehrenbacher, A., Schmale, J.R., Zinn, M.R., & Pfefferkorn, F.E., 2014. Measurement of Tool-Workpiece Interface Temperature Distribution in Friction Stir Welding. Journal of Manufacturing Science and Engineering, 136(2), pp. 021009-1 to 021009-8

Grujicic, M. , Arakere G., Yalavarth H.V, He, C.-F. Yen C-F and Cheeseman B.A, 2010. Modeling of AA5083 Material-Microstructure Evolution During Butt Friction-Stir Welding. Journal of Materials Engineering and Performance, 19(5), pp.672–684.

Hasan, A.F., Bennett, C.J., & Shipway, P.H., 2015, A numerical comparison of the flow behaviour in Friction Stir Welding (FSW) using unworn and worn tool geometries. Materials & Design, 87, pp. 1037–1046.

Idagawa, H.S., Santos, T.F.A., & Ramirez, A. J,. 2014. Differential Evolution algorithm applied to FSW model calibration. Journal of Physics: Conference Series, 490, 012215 (1-5).

Jacquin, D., de Meester B., Simar A., Deloison D., Montheillet F., Desrayaud C. , 2011. A simple Eulerian thermomechanical modeling of friction stir welding. Journal of Materials Processing Technology, 211(1), pp.57–65.

Khandkar, M.Z.H., Khan, J. A. & Reynolds, A. P., 2003. Prediction of temperature distribution and thermal history during friction stir welding: input torque based model. Science and Technology of Welding and Joining, 8(3), pp.165–174.

Samuels, L. E, 1999, Light microscopy of carbon steel, ASM International ©, USA.

Lienert T. J., W. L. Stellwag, JR., B. B. Grimmett and R. W. Warke, 2003. Friction Stir Welding Studies on Mild Steel. , Welding Journal, 82(1), pp.s1–s9.
Masteel.co.uk/dh36.htm 2015.

Megastir. 2013 ,Friction Stir Welding of high melting temperature materials , http://megastir.com/products/tools/fsw_tool.aspxpdf.

McPherson N.A., Galloway A.M., Cater S.R., Hambling S.J., 2013, Friction stir welding of thinDH36 steel plate. Sci. Tech. Weld Join;18(5), pp.441–50.

Micallef, D., Camilleri, D., Toumpis, A., Galloway, A., & Arbaoui, L. (2015). Local heat generation and material flow in friction stir welding of mild steel assemblies. J Materials: Design and Applications, 230 (2), pp. 586-602.

Morisada, Y., Imaizumi, T., Fujii, H., Matsushita, M., & Ikeda, R. (2014). Three-Dimensional Visualization of Material Flow During Friction Stir Welding of Steel and Aluminum. Journal of Materials Engineering and Performance, 23(November), 4143–4147.

Nandan R., DebRoy T. and Bhadeshia H. K. D. H., 2008, Recent Advances in Friction Stir Welding – Process, Weldment Structure and Properties, Progress in Materials Science, 53, 980-1023.

Nandan R. , Roy G.G. , Lienert T.J., Debroy T., 2007. Three-dimensional heat and material flow during friction stir welding of mild steel. Acta Materialia, 55(3), pp.883–895.

Nandan, R., Roy, G.G. , Debroy, T., 2006. Numerical Simulation of Three-Dimensional Heat Transfer and Plastic Flow During Friction Stir Welding. Metallurgical and materials transaction A , 37A, pp1247-1259.
Reynolds, A. P., Tang, W., Posada, M. and DeLoach, J., 2003, Friction stir welding of DH36 steel, Science and Technology of Welding and Joining, Vol. 8, No. 6, pp.455-460.

Schmidt, H. & Hattel, J., 2005. Modelling heat flow around tool probe in friction stir welding. Science and Technology of Welding and Joining, 10(2), pp.176–186.

Schmidt H.N.B., Dickerson T.L., Hattel J.H., (2006), Material flow in butt friction stir welds in AA2024-T3. Acta Mater. 54, pp. 1199–1209.

Stevenson R., Toumpis A, Galloway A, 2015, Defect tolerance of friction stir welds in DH36 steel, Material and design, 87, pp. 701-711.

Subrata Pal, Phaniraj M.P., 2015, Determination of heat partition between tool and workpiece during FSW of SS304 using 3D CFD modelling, Journal of Materials Processing Technology, (222) , pp. 280–286.

Thomas W.M., Threadgill P.L., Nicholas E.D., 1999, Feasibility of friction stir welding steel, Science and Technology of Welding and Joining, 4 (6), 365-372.

Toumpis A. Gallawi A., Polezhayeva H., Molter L., 2015, Fatigue assessment of friction stir welded DH36 steel, in Friction stir welding and procedding VIII, Ed. by R.S. Mishra, M.W. Mahoney, Y. Sato, and Y. Hovanski, The Minerals, Metals & Materials Society, pp. 11-19.

Toumpis A. Gallawi A., Cater S., Molter L., 2014(a), A techno-economic evolution of friction stir welding of DH36 steel, 10th Friction Stir Welding Symposium ,10th FSWS, 20-22/05/2014, Beijing pp.1-11.

Toumpis, A. ,Gallawi A., Cater S., McPherson N., 2014(b), Development of a process envelope for friction stir welding of DH36 steel – A step change. Materials & Design, 62, pp.64–75.

Toumpis A. I., Gallawi A.M., Arbaoui L., Poletz N., 2014(c) , Thermo-mechanical deformation behaviour of DH36 steel during friction stir welding by experimental validation and modelling, Science and Technology of Welding and Joining, Vol 19, Issue 8, pp. 653-663.

Ulysse P., 2002, Three-dimensional modeling of the friction stir-welding process, International Journal of Machine Tools & Manufacture 42, pp. 1549–1557.

Xiaocong He , Fengshou Gu, Andrew Ball, 2014, A review of numerical analysis of friction stir welding, Progress in Materials Science, 65, pp. 1–66.

Zhang, Z. , Zhang, H.W., 2009, Numerical studies on the effect of transverse speed in friction stir welding. Materials & Design, 30(3), pp.900–907.

Zhang, Z. , Zhang, H.W., 2014, Solid mechanics-based Eulerian model of friction stir welding, Int J Adv Manuf Technol, 72, pp. 1647–1653.